

# Free-space coherent optical communication with orbital angular, momentum multiplexing/demultiplexing using a hybrid 3D photonic integrated circuit

Binbin Guan,<sup>1</sup> Ryan P. Scott,<sup>1,\*</sup> Chuan Qin,<sup>1</sup> Nicolas K. Fontaine,<sup>2</sup> Tiehui Su,<sup>1</sup> Carlo Ferrari,<sup>3</sup> Mark Cappuzzo,<sup>3</sup> Fred Klemens,<sup>3</sup> Bob Keller,<sup>3</sup> Mark Earnshaw,<sup>3</sup> and S. J. B. Yoo<sup>1</sup>

<sup>1</sup>Department of Electrical and Computer Engineering, University of California, Davis, CA 95616, USA

<sup>2</sup>Bell Laboratories, Alcatel-Lucent, 791 Holmdel Rd, Holmdel, NJ 07733, USA

<sup>3</sup>Bell Laboratories, Alcatel-Lucent, 600 Mountain Ave, Murray Hill, NJ 07974, USA

\*[rpscott@ucdavis.edu](mailto:rpscott@ucdavis.edu)

**Abstract:** We demonstrate free-space space-division-multiplexing (SDM) with 15 orbital angular momentum (OAM) states using a three-dimensional (3D) photonic integrated circuit (PIC). The hybrid device consists of a silica planar lightwave circuit (PLC) coupled to a 3D waveguide circuit to multiplex/demultiplex OAM states. The low excess loss hybrid device is used in individual and two simultaneous OAM states multiplexing and demultiplexing link experiments with a 20 Gb/s, 1.67 b/s/Hz quadrature phase shift keyed (QPSK) signal, which shows error-free performance for 379,960 tested bits for all OAM states.

©2013 Optical Society of America

**OCIS codes:** (060.1660) Coherent communications; (050.4865) Optical vortices; (060.4230) Multiplexing; (130.2755) Glass waveguides.

---

## References and links

1. P. J. Winzer, "High-spectral-efficiency optical modulation formats," *J. Lightwave Technol.* **30**(24), 3824–3835 (2012).
2. R. Essiambre, G. Kramer, P. J. Winzer, G. J. Foschini, and B. Goebel, "Capacity limits of optical fiber networks," *J. Lightwave Technol.* **28**(4), 662–701 (2010).
3. L. Allen, M. W. Beijersbergen, R. J. C. Spreeuw, and J. P. Woerdman, "Orbital angular momentum of light and the transformation of Laguerre-Gaussian laser modes," *Phys. Rev. A* **45**(11), 8185–8189 (1992).
4. A. M. Yao and M. J. Padgett, "Orbital angular momentum: origins, behavior and applications," *Adv. Opt. Photonics* **3**(2), 161–204 (2011).
5. N. Bozinovic, Y. Yue, Y. Ren, M. Tur, P. Kristensen, H. Huang, A. E. Willner, and S. Ramachandran, "Terabit-scale orbital angular momentum mode division multiplexing in fibers," *Science* **340**(6140), 1545–1548 (2013).
6. M. W. Beijersbergen, R. P. C. Coerwinkel, M. Kristensen, and J. P. Woerdman, "Helical-wavefront laser beams produced with a spiral phaseplate," *Opt. Commun.* **112**(5–6), 321–327 (1994).
7. J. Wang, J.-Y. Yang, I. M. Fazal, N. Ahmed, Y. Yan, H. Huang, Y. Ren, Y. Yue, S. Dolinar, M. Tur, and A. E. Willner, "Terabit free-space data transmission employing orbital angular momentum multiplexing," *Nat. Photonics* **6**(7), 488–496 (2012).
8. J. Leach, M. J. Padgett, S. M. Barnett, S. Franke-Arnold, and J. Courtial, "Measuring the orbital angular momentum of a single photon," *Phys. Rev. Lett.* **88**(25), 257901 (2002).
9. T. Su, R. P. Scott, S. S. Djordjevic, N. K. Fontaine, D. J. Geisler, X. Cai, and S. J. B. Yoo, "Demonstration of free space coherent optical communication using integrated silicon photonic orbital angular momentum devices," *Opt. Express* **20**(9), 9396–9402 (2012).
10. N. K. Fontaine, C. R. Doerr, and L. Buhl, "Efficient multiplexing and demultiplexing of free-space orbital angular momentum using photonic integrated circuits," in *Optical Fiber Communication Conference, OSA Technical Digest* (Optical Society of America, 2012), OTu11.2.
11. J. Sun, E. Timurdogan, A. Yaacobi, E. S. Hosseini, and M. R. Watts, "Large-scale nanophotonic phased array," *Nature* **493**(7431), 195–199 (2013).
12. B. Guan, R. P. Scott, N. K. Fontaine, T. Su, C. Ferrari, M. Cappuzzo, F. Klemens, B. Keller, M. Earnshaw, and S. J. B. Yoo, "Integrated optical orbital angular momentum multiplexing device using 3-D waveguides and a silica PLC," in *CLEO: 2013, OSA Technical Digest* (online) (Optical Society of America, 2013), CTu1L.4.
13. R. P. Scott, B. Guan, C. Qin, N. K. Fontaine, T. Su, C. Ferrari, M. Cappuzzo, F. Klemens, B. Keller, M. Earnshaw, and S. J. B. Yoo, "Free-space coherent optical communication demonstration using a 3D photonic

- integrated circuit device for orbital angular momentum multiplexing/demultiplexing,” in *European Conference and Exhibition on Optical Communication (ECOC)*, OSA Technical Digest (Optical Society of America, 2013), Tu.3.B.2.
14. Y. Nasu, M. Kohtoku, and Y. Hibino, “Low-loss waveguides written with a femtosecond laser for flexible interconnection in a planar light-wave circuit,” *Opt. Lett.* **30**(7), 723–725 (2005).
  15. R. R. Thomson, H. T. Bookey, N. D. Psaila, A. Fender, S. Campbell, W. N. Macpherson, J. S. Barton, D. T. Reid, and A. K. Kar, “Ultrafast laser inscription of a three-dimensional fan-out device for multicore fiber coupling applications,” in *Quantum Electronics and Laser Science Conference* (Optical Society of America, 2008).
  16. A. V. Oppenheim, A. S. Willsky, and S. H. Nawab, *Signals and Systems* (Prentice-Hall, 1983), Vol. 2.
  17. A. Himeno, K. Kato, and T. Miya, “Silica-based planar lightwave circuits,” *IEEE J. Sel. Top. Quantum Electron.* **4**(6), 913–924 (1998).
  18. K. Okamoto, *Fundamentals of Optical Waveguides* (Elsevier, 2010).
  19. W. Steinchen and L. X. Yang, *Digital Shearography: Theory and Application of Digital Speckle Pattern Shearing Interferometry* (SPIE, 2003), Vol. 100.
  20. M. Kawachi, “Silica waveguides on silicon and their application to integrated-optic components,” *Opt. Quantum Electron.* **22**(5), 391–416 (1990).
  21. J. G. Proakis and M. Salehi, *Digital Communications*, 5th ed. (McGraw-Hill, 2008).
  22. I. Kaminow, T. Li, and A. E. Willner, *Optical Fiber Telecommunications VB: Systems and Networks* (Academic, 2010).
  23. S. J. Savory, “Digital filters for coherent optical receivers,” *Opt. Express* **16**(2), 804–817 (2008).
  24. A. Papoulis and S. U. Pillai, *Probability, Random Variables, and Stochastic Processes* (McGraw-Hill, 2002).
  25. D. Mitić, A. Lebl, and Ž. Markov, “Calculating the required number of bits in the function of confidence level and error probability estimation,” *Serbian J. Electr. Eng.* **9**(3), 361–375 (2012).
  26. T. Mizuochoi, “Forward error correction,” in *High Spectral Density Optical Communication Technologies*, M. Nakazawa, K. Kikuchi, and T. Miyazaki, eds. (Springer, 2010), pp. 303–333.
- 

## 1. Introduction

The explosive growth of data traffic has transformed the landscape of modern telecommunication networks. Initially, the remarkable increases in capacity demands were successfully met by deployment of wavelength-division-multiplexing (WDM) technologies, which increased communication capacity from 10 Gb/s to multiple Tb/s on a single mode fiber. Recent optical networking advances have addressed optical communications with high spectral efficiency beyond 1~10 b/s/Hz employing advanced modulation formats. The steady increases in spectral efficiency reported for high capacity transmission systems, which has reached 100 Tb/s capacity and 10 b/s/Hz spectral efficiency [1]. However, it is extremely difficult to support such high spectral efficiency over a long distance due to the nonlinear Shannon limit [2] of the fiber-optic channel for even moderate (~500 km) transmission distances. Space-division-multiplexing (SDM) becomes an attractive and practical technique to provide an additional degree of freedom for increasing the spectral efficiency and communication capacity [1]. One such SDM method on orbital angular momentum (OAM) [3] has generated great interest because of its relative simple employment of cylindrically symmetric modes. The light beam carrying orbital angular momentum exhibits an azimuthal phase variation of  $\varphi(r, \phi) = \exp(i\ell\phi)$ , where  $\phi$  is the azimuthal angle and  $\ell$  the charge number or OAM state; a positive or negative integer. The handedness of this helical phase front is determined by the sign of the charge number  $\ell$  and a non-zero state OAM beam leads to a phase singularity on the beam axis [4]. Hence, the amplitude along the beam axis vanishes, and the center of the OAM beam is dark. Compared to a spin mode (i.e., polarization), the light beam can in principle support an infinite number of OAM states at the same time (subject to the limitation imposed by the signal to noise ratio). Therefore, OAM has the potential to significantly improve the spectral efficiency or photon efficiency of free-space and fiber optical communications [5]. In addition, the inherent orthogonality of the various OAM states may reduce crosstalk, resulting in reduced reliance on digital signal processing (DSP) compared to cases employing standard multiple-input and multiple-output (MIMO) methods. For instance, Bozinovic et al. [5] have recently demonstrated OAM transmission over 1.1-km of fiber for up to 10 OAM states without the use of MIMO.

The early work of Allen [3] on OAM was followed by a number of papers experimentally demonstrating OAM generation, sorting, multiplexing, and demultiplexing. Typical

approaches utilize holograms [6], spatial light modulators (SLMs) [7], dove prisms [8], and other bulk optics. However, practical SDM systems greatly benefit from integrated optics on a robust platform, especially when combined with coherent optical communications. Our group demonstrated silicon photonic OAM multiplexing and demultiplexing devices based on a free propagation region employing a Rowland circle and waveguide apertures with grating structures [9], and a number of other groups have also provided alternative integrated 2D photonic circuits for creating spatial modes [10, 11]. Such structures induce relatively large losses and polarization dependent losses that impede their broad use in transmission systems.

In this paper, we follow up on our first reports [12, 13] of a 3D photonic integrated circuit capable of multiplexing/de-multiplexing OAM states. The circuit supports up to 15 OAM states, with both TE and TM polarizations and relatively low loss performance at 1.55  $\mu\text{m}$ . The compact design and single-mode interface easily connect with other high speed optical components for future on-chip integration. This paper is organized as follows, Section 2 discusses the device's design and operating principles, Section 3 provides device characterization results, Section 4 and 5 present free-space transmission demonstration results, and Section 6 is the conclusion.

## 2. Orbital angular momentum device design and operating principle

Figure 1 shows a conceptual diagram of a photonic integrated circuit (PIC) for OAM beam generation and multiplexing. On the left side, each single-mode waveguide input corresponds to an OAM state ( $\ell = -2$  through  $+2$  shown). The input light beams pass through the free-propagation region (FPR) employing the Rowland circle, where they laterally expand and the wavefronts acquire a linear phase tilt based on the input waveguide position. At the output side of the FPR, the phase-matched waveguides sample the wavefront and maintain the phase relationship. A geometrical transformation is then necessary for conversion of the linear phase tilt to azimuthal phase variations at the output apertures. If multiple inputs are illuminated simultaneously, the OAM states are multiplexed, and they overlap spatially at the output apertures. On the other hand, when operated in reverse, the 3D waveguides' circular-patterned apertures can sample and retrieve spatially overlapped OAM states, and as a result, the demultiplexed signal can be detected at different output waveguides of the silica PLC.

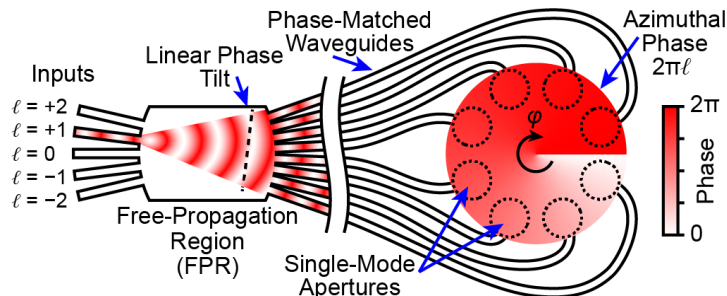


Fig. 1. Concept of the OAM photonic integrated circuit for multiplexing or demultiplexing free-space OAM beams.

In this work, laser inscribed 3D waveguides [14, 15] perform the geometrical conversion, and at the output of the 3D waveguide apertures, we have a discretely sampled optical beam with the correct azimuthal phase for each of the OAM states. OAM states can be fully recovered if the sampling of the OAM state azimuthal phase distribution satisfies Nyquist sampling theory [16]. Referring to Fig. 1, if we consider each output aperture as a spatial beam sample and those samples are evenly distributed around the azimuthal coordinate, the number of supported OAM states depends on the number of beam samples (i.e., apertures or waveguides). Therefore, at least  $2N$  waveguides are required for the generation of  $2N$  OAM states (e.g., from  $\ell = -N + 1$  to  $\ell = +N$ , including  $\ell = 0$ ). Since this multiplexing technique does not suffer from  $1 \times N$  splitting/combining losses, with photonic integration, scaling the

number of the waveguides and increasing the number of supported OAM states to very large numbers without large losses is straightforward. However, OAM state crosstalk emerges as the practical limit for device implementation.

Figure 2 shows a conceptual drawing of our implementation of Fig. 1, where the OAM hybrid integrated device is composed of a silica PLC and a 3D waveguide circuit. The silica PLC has 17 waveguide inputs where 15 are used to create linearly tilted wavefronts that correspond to unique OAM states (i.e., from  $\ell = -7$  to  $\ell = +7$ ), and the additional 2 input waveguides are used for device characterization. The FPR is implemented as a star coupler and performs a Fourier transform so that the unique angle of the input waveguide creates a wavefront with a specific linear phase tilt. The FPR has 17 waveguide outputs that sample the wavefront, but only the first 16 waveguides are used to create the OAM beam (the 17th waveguide's phase is always the same as the first waveguide and is used for characterization). There are electrical heaters on each output waveguide after the FPR to provide the phase error correction (PEC) necessary for correcting the unintended phase variations rising from both fabrication errors and length variations in the 3D waveguides. Here we define the path length differences between 3D waveguides as length variations. The waveguides on the silica PLC use a  $\Delta n$  of 2% [17]. Figure 3(a) shows a photo of the fabricated PLC which is 15-mm long and it has a 127- $\mu\text{m}$  pitch for both the input and the output waveguides. Figure 3(b) shows the output light beam intensities captured by an infrared camera.

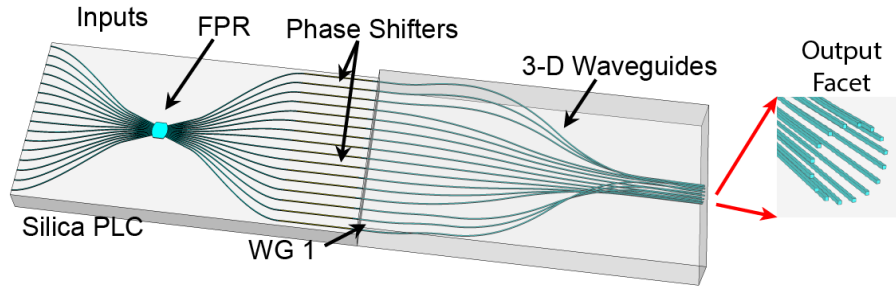


Fig. 2. Conceptual view of the hybrid photonic integrated device for OAM state multiplexing and demultiplexing.

The right part of Fig. 2 shows a conceptual drawing of the 3D waveguide circuit with a magnified view of output facet. 3D waveguide circuit was fabricated at a commercial foundry by direct laser writing of the optical waveguides in a borosilicate glass. The fabrication technique uses focused femtosecond laser pulses to permanently increase the refractive index via multi-photon absorption, which occurs directly inside a transparent dielectric material. Three-axis variation of the substrate during the laser writing enables an accurate fabrication of the 3D waveguides. Figure 3(c) shows a photo of the 3D waveguide circuit's output facet before polishing so that the 16 waveguides are visible. The mode field diameter of each output is  $\sim 10 \mu\text{m}$  (numerical aperture (NA) = 0.1). The center-to-center spacing between neighboring outputs is kept at  $40 \mu\text{m}$  to minimize coupling between adjacent waveguides. The circular pattern diameter is  $204 \mu\text{m}$  and the length of the 3D waveguide is 19 mm. Over this distance, the 2D-array waveguides can carefully transit to their 3D circular geometry while keeping bending losses negligible. The waveguides are pathlength matched to within  $40 \mu\text{m}$ , which provides an operating bandwidth of  $\sim 9 \text{ nm}$  when the heaters on the silica PLC phase match the output waveguides (assuming two identical devices and  $< -10\text{-dB}$  crosstalk). The operating bandwidth is defined as the maximum wavelength range at which the crosstalk for each OAM state is less than  $-10 \text{ dB}$ . The operating bandwidth is based on a simulation of the OAM state crosstalk that uses the wavelength dependent phase errors that arise from the path length difference,  $\varphi_{\text{error}} = 2\pi n_{\text{eff}} \Delta L / \lambda$ , where  $n_{\text{eff}}$  is 1.49. Figure 3(d) shows the measured output intensities of the 3D waveguides. The variation in the intensity distribution occurs mainly within the silica PLC where the illumination of the outer-most FPR output

waveguides is less than the center waveguides. The input power from any one of the  $N$  input waveguides is radiated to the FPR and it is received by the output waveguide array. The radiation pattern at the output side of the FPR is the Fraunhofer pattern (Fourier transform) of the field profile at the input side FPR-array interface. The FPR parameters, such as the aperture angle, radius of the FPR region and input/output waveguide taper shapes, were optimized by using beam propagation method (BPM) simulations to concurrently try to maximize the output power, splitting uniformity, and desired phase conditions [18]. Since OAM state crosstalk arises from the combination of phase errors and amplitude (or intensity) variations from each waveguide in the hybrid device, variations in the intensity distribution may decrease the performance of the hybrid devices. Further investigations are needed to reduce the variations in intensity distribution, as well as the excess loss in future silica PLC designs.

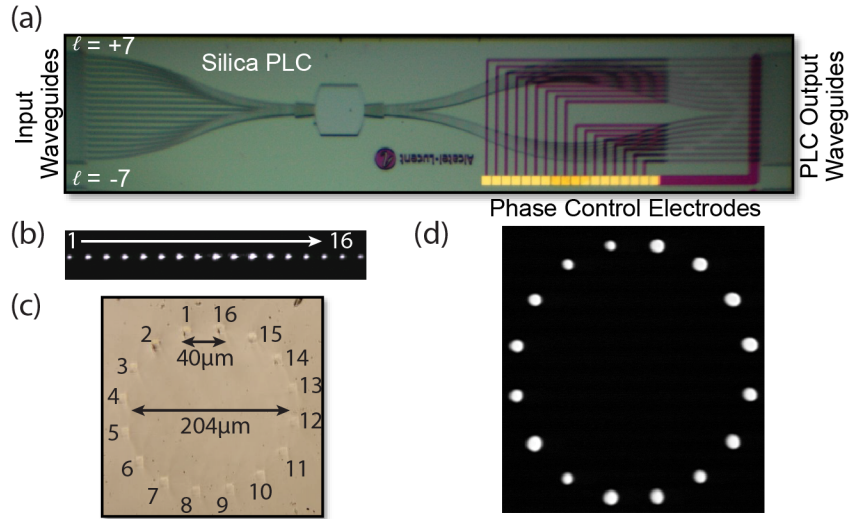


Fig. 3. Integrated device details. (a) Silica PLC image. (b) Measured mode profile of the silica PLC output waveguides (17 outputs). (c) 3D waveguide output facet image before polishing. (d) Measured mode profile of the light beams at the output of the 3D waveguides.

### 3. Device characterization

Figure 4(a) shows the simulated loss of the silica PLC due to the FPR region design and the measured total loss of the silica PLC with input OAM state 0. The measured loss shows less variation than the simulation predicts, possibly due to fabrication errors. Figure 4(b) presents the excess loss for the silica PLC using the OAM state 0 input and the insertion loss for the 3D waveguides. The measurements were made using cleaved single mode fibers and index matching fluid and the PLC's excess loss does not include the simulated splitting loss. Excess loss is defined as the difference between the measured loss and expected (simulated) loss. The excess loss of the silica PLC is  $\sim 3.5$  dB and mainly arises from fabrication errors and mode mismatch between the single mode fibers and PLC waveguide (i.e., to avoid risk of damage, there was always a gap between the fiber and facet). As mentioned previously, the silica PLC loss [Fig. 4(a)] is highest for the outer-most waveguides (i.e., lowest and highest waveguide numbers) due to the FPR design, while the 3D waveguides' loss variation is much smaller at  $< 0.6$  dB. The measured total excess loss of the hybrid device is  $\sim 7.5$  dB with a variation of 1.5 dB across all inputs.

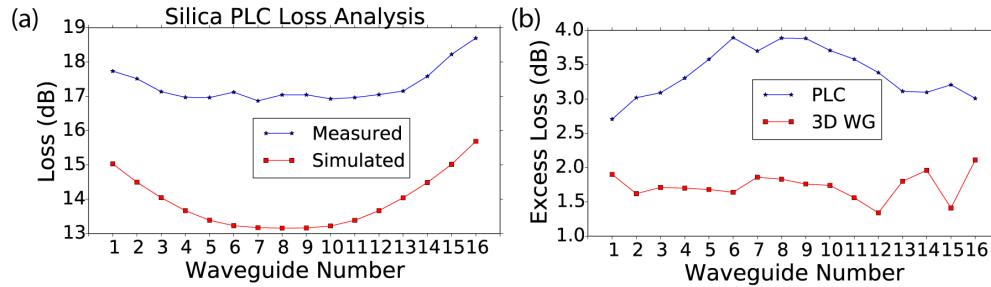


Fig. 4. (a) Measured and simulated loss distribution for the output waveguides of the silica PLC (OAM state 0 as input). (b) Measured excess loss for the silica PLC and insertion loss of the 3D waveguides.

To characterize the phase of the OAM hybrid device outputs, we used a technique based on spatial shearing interferometry [19] where a tilted reference beam with flat spatial phase is interfered with a signal beam that has a known spatial intensity but unknown spatial phase. Separately measuring the signal beam, reference beam, and their resulting interferogram, allows retrieval of the unknown spatial phase. Figure 5(a) shows the measurement arrangement where the output of the hybrid device is imaged onto an infrared camera with a magnifying lens ( $f_1 = 4.51$  mm and  $f_2 = 100$  mm) arrangement when only one input of the silica PLC was illuminated at a time. We used polarization-maintaining (PM) fiber after the polarizer to insure TE polarization at the device input and reference beam output. The magnified image of hybrid device output interfered with the linear tilted reference beam, resulting in the generation of an interference pattern on the infrared camera. We used offline digital signal processing of the images to retrieve both the amplitude and the phase (modulo  $2\pi$  rad) of each waveguide output with a measurement update rate of  $\sim 0.5$  Hz.

Using the fast updating spatial phase measurements, we proceeded to correct the phase errors of the hybrid device. The upper color maps in Fig. 5(b) show the measured near-field pattern (intensity and phase of the waveguide outputs) for OAM state 0 before any PEC was applied. The phase of each waveguide output is random due to the phase errors from both the silica PLC and the 3D waveguides. After applying voltages to the electrical heaters [20], the lower color maps in Fig. 5(b) show that we could correct all of the phase errors and equalize the phases of the waveguide outputs (OAM state 0 has no azimuthal phase variation). The measured electrical power for a  $\pi$  rad phase shift (i.e.,  $P_\pi$ ) was  $\sim 400$  mW (no heat isolating trenches were used [18]). The silica PLC was set on an aluminum block that was temperature stabilized to  $30^\circ\text{C}$  and the PLC was held in place by the pressure of the multiprobe used to access the electrical connections. Although the temperature stabilization of the aluminum block worked well with or without the PEC applied, we suspect that varying air currents across the device's surface may impact the local temperatures of the PLC heater regions and limit the phase stability. A fully packaged device may further improve its phase stability. Figure 5(c) shows a line plot of the phase data in Fig. 5(b) for easy comparison. The measured result with PEC matches the theoretical phase distribution of OAM state 0 well.

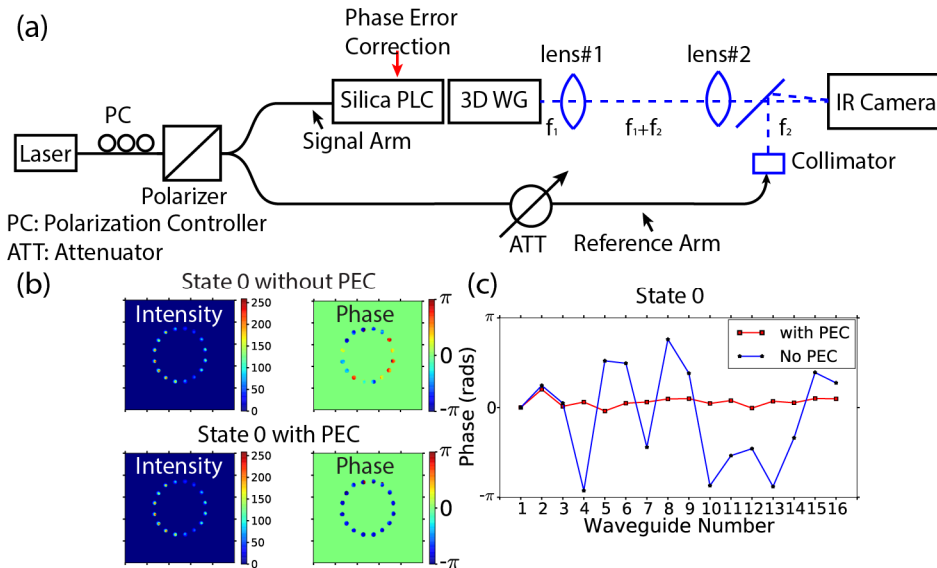


Fig. 5. (a) Experimental arrangement for OAM device intensity and phase characterization. (b) Near-field intensity and phase before and after phase-error correction is applied for OAM state 0 (flat phase). (c) Line plot of the measured near-field phase shown in (b).

The near-field output phase was then measured in a similar way for all of the OAM states through the illumination of one input waveguide of the silica PLC at a time (from  $\ell = -7$  to  $\ell = +7$ ). Figure 6(a) summarizes the results for all of the OAM states where PEC adjustments were made only for OAM state 0. OAM states with opposite sign show the correct change in azimuthal phase rotation. For OAM states  $+7$  and  $-7$ , the phase is sampled by nearly a factor of 2 as a result of the 16 waveguides. Therefore, it is approaching the Nyquist sampling theory limitation which occurs for OAM states  $+8$  and  $-8$  where each waveguide has a relative phase of  $0$  or  $\pi$  and it is not possible to unambiguously determine the OAM state. Figure 6(c) shows the unwrapped phase plot versus waveguide output number for all of the OAM states. The result shows clearly that, for each OAM state, the phase is the product of  $2\pi$  and the OAM charge number  $\ell$ .

The characterization results demonstrate that the hybrid device can be used for OAM state multiplexing/demultiplexing, with low excess loss and repeatable performance. Since this multiplexing technique does not suffer from  $1 \times N$  splitting/combining losses, with photonic integration, scaling the number of the waveguides and increasing the number of supported OAM states to very large numbers without large losses is straightforward.

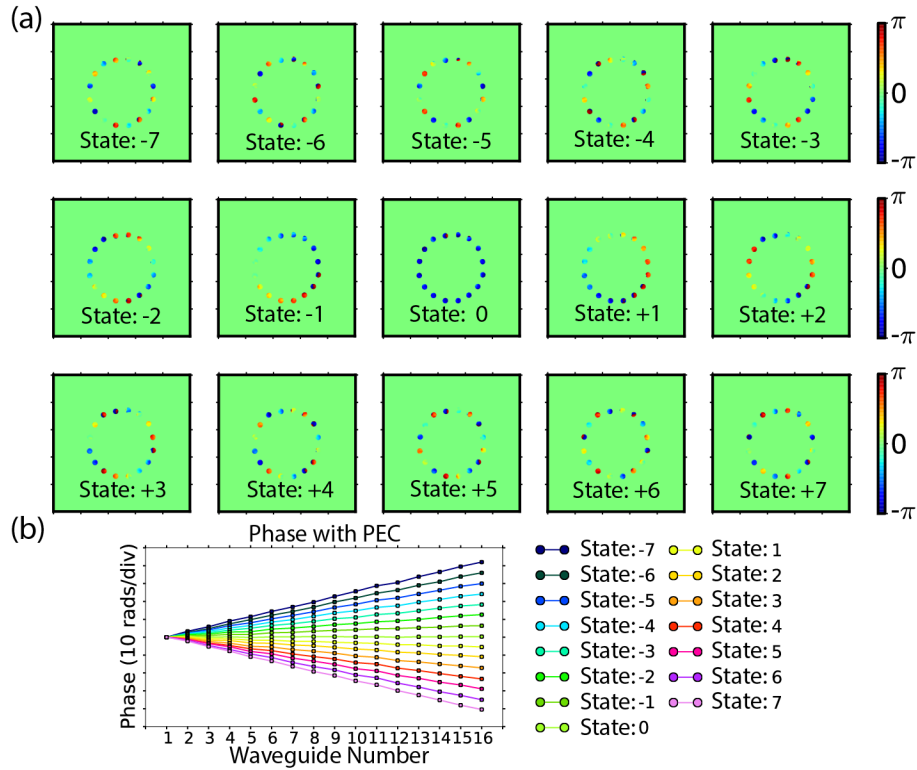


Fig. 6. Integrated photonic circuit OAM state characterization results. (a) OAM state near-field phase pattern as a color map. (b) Line plots of the measured and unwrapped phase for each OAM state.

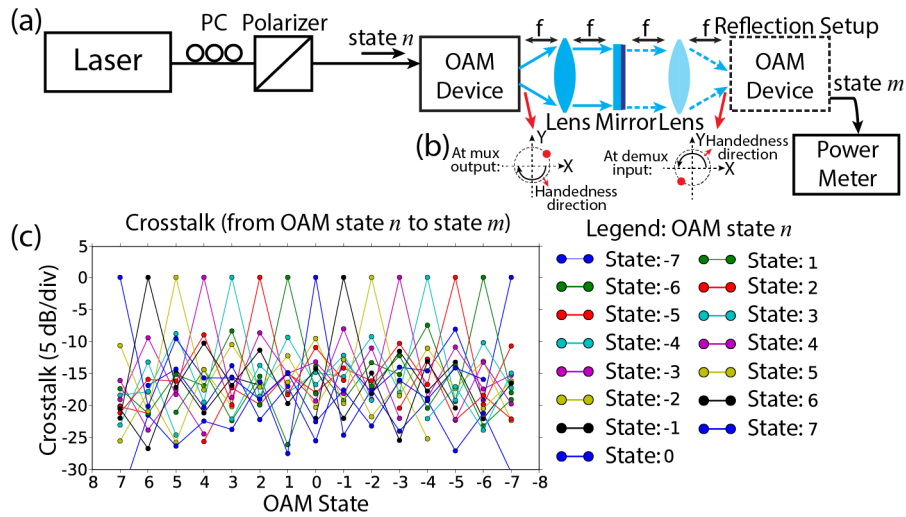


Fig. 7. (a) Crosstalk experimental setup. (b) An example of how the lens and mirror reflection change the beam pattern. (c) Measured crosstalk for OAM state  $n$  to  $m$ .

To measure the crosstalk between one OAM state and all other states, we used a single hybrid device for multiplexing and demultiplexing. Figure 7(a) shows the retro-reflection based setup used to measure the crosstalk. The retro-reflection setup builds a  $4f$  imaging system with one aspheric lens ( $f = 4.51$  mm) and one mirror. In this particular arrangement,

light at the  $+l$  input of the silica PLC (OAM state  $+l$ ) comes out at the  $-l$  output of the silica PLC, because the mirror reverses the propagation direction for the OAM beam. As Fig. 7(b) illustrates, the lens and mirror also rearrange the beam to different 3D waveguides while changing the handedness of the azimuthal phase. Therefore, when we illuminated input +1 of the silica PLC, we expected to receive a peak value at input -1 on the same silica PLC. This behavior is verified by Fig. 7(c) which shows measurements for the crosstalk between one OAM state and all other states. The crosstalk was measured as the normalized fiber-to-fiber loss from input  $n$  to output  $m$  ( $n \neq m$ ) for the multiplexer/demultiplexer pair. The maximum measured crosstalk is approximately  $-8$  dB which is somewhat worse when compared to the measured OAM spectrum (mode purity) of a single pass through the device (Fig. 2(f) of [12]).

#### 4. Free-space coherent optical communication link experiment

We performed an OAM state link experiment with a 10-GBd quadrature phase shift keyed (QPSK) signal. Figure 8 shows the experimental testbed schematic which includes the free-space coherent SDM link of 1.8 cm that is based on a retro-reflecting  $4-f$  imaging system. In the setup, we used one hybrid OAM device as both the OAM multiplexer and demultiplexer. The transmitter used an external cavity laser (ECL) with a linewidth of 100 kHz and tuned to 1546 nm. A portion of the laser output was sent to the receiver after an acousto-optic modulator (AOM) frequency shifted the carrier by 35 MHz. An electrical arbitrary waveform generator (EAWG) drove the I/Q modulator to generate a 10-GBd QPSK signal, with a  $2^7-1$  pseudorandom bit sequence (PRBS). Offline digital signal processing (DSP) created a pre-emphasized (shaped) QPSK signal with a 10-GHz, 6-dB bandwidth Nyquist filter (roll-off factor is 0.2) [21]. As a result, the single channel spectral efficiency was 1.67 b/s/Hz [2]. We included an erbium-doped fiber amplifier (EDFA) to increase the output signal power from the I/Q modulator to 15 dBm. Since the transmitter, noise loader, and receiver were located in a room separate from the OAM device, a 25-m fiber, polarization stabilizer, and EDFA were used between the transmitter and OAM device. An attenuator before the OAM device was used to optimize the input power and a 2-m fiber temporally decorrelated the signal patterns on the two inputs when we transmitted two OAM states simultaneously.

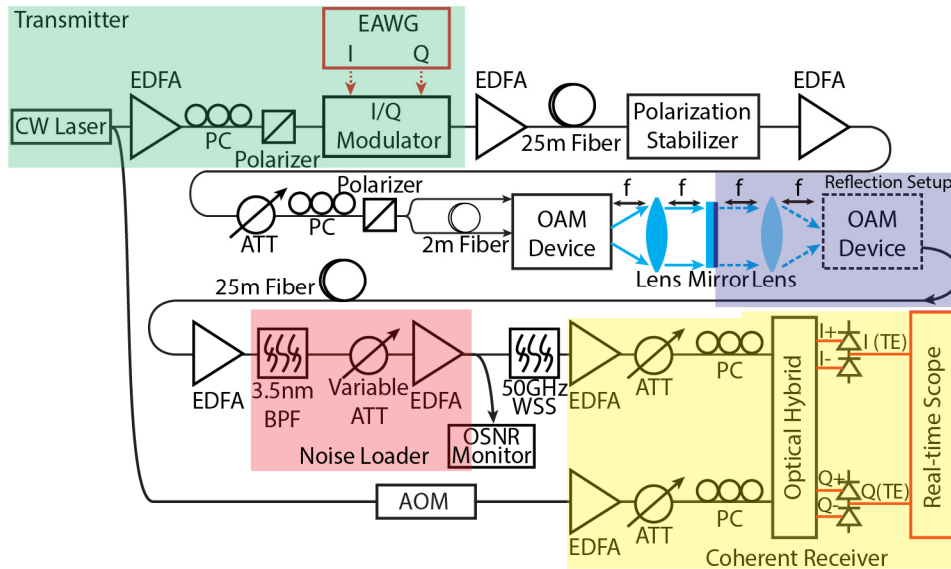


Fig. 8. 10-GBd QPSK link experimental arrangement using a retro-reflecting free-space link. EAWG: electrical arbitrary waveform generator. EDFA: erbium-doped fiber amplifier. PC: polarization controller. ATT: attenuator. BPF: bandpass filter. AOM: acousto-optic modulator. WSS: wavelength selective switch.

After demultiplexing, the signal passed through 25 m of fiber before it was amplified by an EDFA with a 3.5-nm bandpass filter (BPF) to minimize the out-of-band noise. We varied the optical signal-to-noise ratio (OSNR) by using a variable optical attenuator and an EDFA directly after the BPF. On the receiver side, the signal, as well as a 35-MHz frequency shifted local oscillator (LO), enters a polarization diversity optical hybrid. Both the real and the imaginary parts of the coherently detected signal were collected by a 50 GS/s real-time oscilloscope (16-GHz, 3-dB bandwidth).

We applied offline DSP to evaluate bit-error-rate (BER) performance for the received data using the following steps. The DSP first extracted the clock tone from the Fourier transform of the received magnitude-squared signal in the time domain [22]. Next, the data were resampled to 20 GS/s. A 13-tap finite impulse response (FIR) filter adapted by a constant modulus algorithm [23] constituted an adaptive equalizer, which was applied to the resampled waveform. Lastly, carrier phase recovery used the power-of-four average method [22].

Figure 9(a) shows the individual BER performance for OAM states from  $\ell = +1, +2, \dots, +7$  to  $\ell = -1, -2, \dots, -7$  measured by varying the OSNR. The blue curve on the left side in Fig. 9(a) shows the theoretical QPSK BER performance with differential decoding based error counting [21]. The green curve shows the back-to-back (b2b) BER performance which has an OSNR implementation penalty of  $\sim 2$  dB at  $\text{BER} = 10^{-3}$ . In our experiment, the back-to-back arrangement directly connects the modulator output to the noise loader and coherent receiver in Fig. 8. For OAM states  $+1, +2, \dots, +7$ , there is a 0.5-dB OSNR penalty when measured at  $\text{BER} = 10^{-3}$ . This small penalty is mainly due to the differences in EDFAs used compared to the back-to-back case. The BER measurement registered no errors detected when the OSNR  $> 14$  dB (received power  $> -36.9$  dBm) with the measured 379,960 bits. This indicates the upper-bound of the BER value to be  $< 10^{-5}$  with 97.7% confidence level [24, 25].

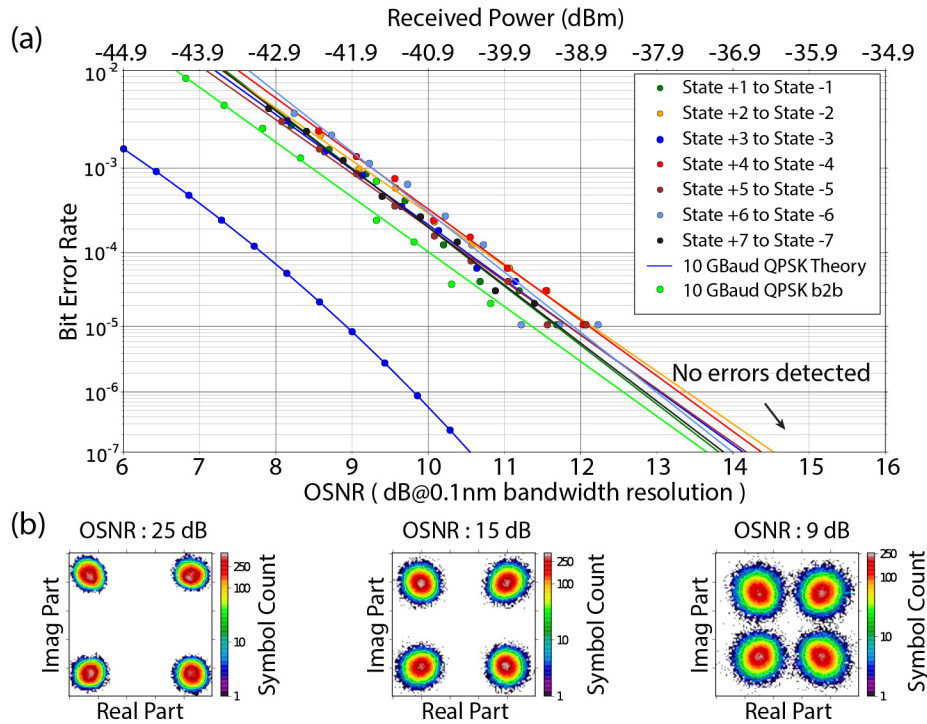


Fig. 9. Link performance for a single transmitted OAM state. (a) BER performance for a 10-GBd QPSK link using OAM states  $+1, +2, \dots, +7$ . (b) Constellation plots at 25 dB, 15 dB and 9 dB OSNR.

We note that hard decision forward-error correction (FEC) such as Reed Solomon method with RS(255,239) coding [26] can bring the raw data with  $\text{BER} < 1.4 \times 10^{-4}$  to error-free performance (i.e.,  $\text{BER} < 10^{-12}$ ). Figure 9(b) shows the constellations for OAM state  $\ell = +1$  at OSNRs of 25 dB, 15 dB and 9 dB, respectively. The slightly non-circular nature of the constellation points arises mainly from the imperfect waveform generation at the transmitter and is not due to the hybrid OAM device since it is present in the back-to-back case as well. Again, when the OSNR is larger than 14 dB, the constellation points are well isolated, which supports the measured error-free performance.

### 5. Two-OAM-state, free-space coherent optical communication link experiment

In the next step, we demonstrated the free-space coherent optical communication link while multiplexing and demultiplexing two simultaneous OAM states. The experimental arrangement is the same as shown in Fig. 8, with the addition of a second illuminated input on the silica PLC. To illustrate performance for various cases, we used the crosstalk measurements in Fig. 7 and chose additional (interfering) states that represented the highest, lowest and average crosstalk scenarios for the OAM states +1 and +3.

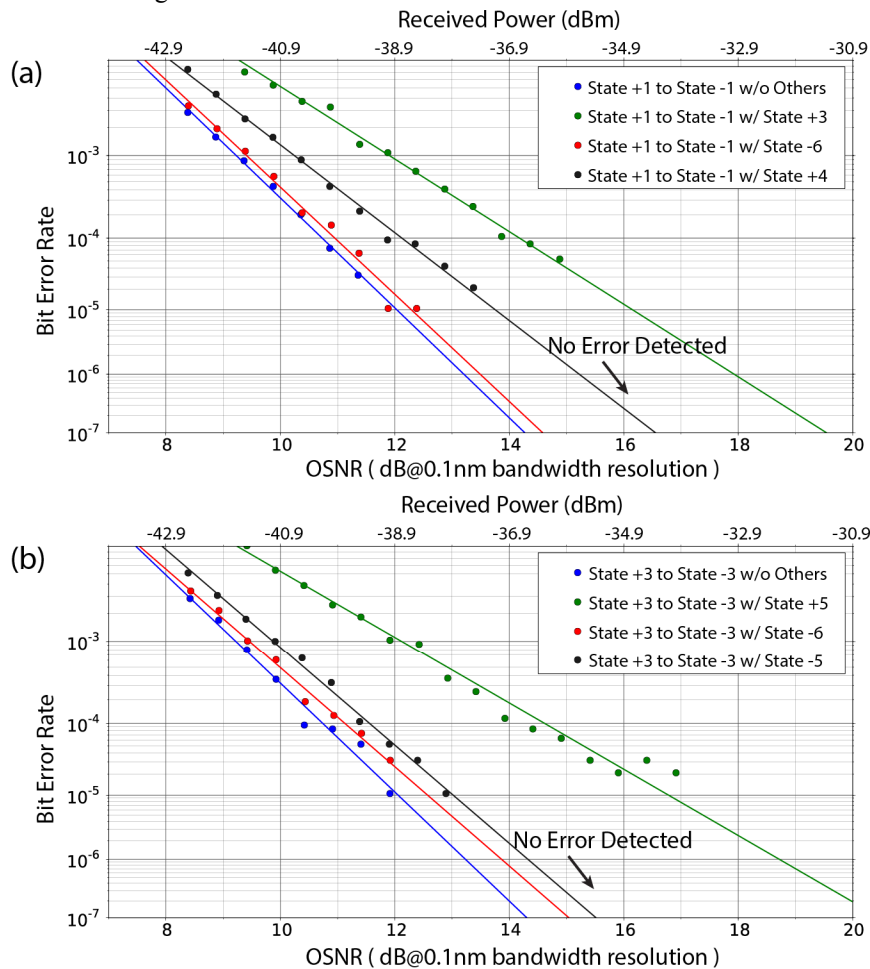


Fig. 10. Link performance for two simultaneous OAM states with varying amounts of crosstalk. (a) BER performance for a 10-GBd QPSK link using OAM state +1 to -1 with, and without, other states (interferer) present. (b) BER performance for a 10-GBd QPSK link using OAM state +3 to -3 with, and without, other states (interferer) present.

Figure 10(a) shows the BER performance (379,960 bits tested) for OAM state + 1, with or without the interfering OAM states of + 3, -6, or + 4. At OSNR > 18 dB (or received power > -32.9 dBm), no errors were recorded with the interfering OAM states. Therefore, error-free performance can be easily achieved with hard decision FEC. The crosstalk between OAM state + 1 and + 3 is -8.38 dB (highest). The crosstalk between OAM state + 1 and -6 is -23.19 dB (lowest). The crosstalk between OAM state + 1 and + 4 is -16.93 dB (average). From the BER performance, the worst case interference (highest crosstalk) between OAM state + 1 and + 3 induces a 2.7-dB OSNR penalty ( $\text{BER} = 10^{-3}$ ) compared to the single state case, while the average and best cases have less than 1-dB OSNR penalty.

Figure 10(b) shows the BER performance for the OAM state + 3, with or without the interfering OAM states + 5, -6, or -5. The crosstalk between OAM state + 3 and + 5 is -8.79 dB (highest). The crosstalk between OAM state + 3 and -6 is -23.87 dB (lowest). The crosstalk between OAM state + 3 and -5 is -17.09 dB (average). Again, the BER performance for the highest case crosstalk (OAM state + 3 and + 5) shows a 2.7-dB OSNR penalty measured at  $\text{BER} = 10^{-3}$  when compared to the case without interfering OAM states. The channels with average or lower crosstalk display less than 1-dB OSNR penalty. Again, at OSNR > 18 dB (or received power > -32.9 dBm), no errors were recorded, which indicates that error-free performance would be easily achieved with hard decision FEC. A fully packaged device with smaller phase errors and better phase stability is expected to reduce the crosstalk and improve the BER performance with multiple OAM states.

## 6. Conclusion

We have demonstrated a hybrid photonic integrated circuit composed of a silica PLC and 3D waveguide PIC which multiplexes and demultiplexes 15 OAM states. Spatial shearing interferometry provided near-field phase characterization to verify that the hybrid OAM produced the correct azimuthal phase for all 15 OAM states. In a retro-reflection arrangement for multiplexing/demultiplexing, the average device crosstalk was -17 dB and the maximum crosstalk was -8 dB. A free-space SDM coherent optical transmission link experiment with a 20-Gb/s QPSK signal and individual OAM beam multiplexing/demultiplexing showed the capability for error-free transmission at OSNR > 14 dB for all of the OAM states, and similar error-free transmission was demonstrated with two simultaneous OAM states for OSNR > 18 dB if hard decision FEC were employed. Future work includes investigating packaging techniques for hybrid device integration with better alignment and phase stability, as well as using multiple devices to perform link experiments with the multiplexing of additional states.

## Acknowledgments

This work was supported in part by DARPA DSO under the contracts HR0011-11-1-0005 and W911NF-12-1-0311.